BALKAN JOURNAL OF ELECTRICAL & COMPUTER ENGINEERING, Vol. 13, No. 4, December 2025

Research Article

High-Efficient Resonant Converter for LED Driver Applications

Mustafa Gokdag, Ozan Gulbudak, Ugur Ufuk Korpe

Abstract **-- In this study, a boost-type Pulse Width Modulation (PWM)-resonant converter is proposed for LED driver applications. Thanks to resonance operation, the converter works with zero current switching for most of the switching instants. Thus, high efficiency can be obtained more easily. It utilizes capacitive energy transfer and offers a reduction in the required inductor size. This leads to converter designs with high power density. The operation principle of the PWM-resonant converter is presented by performing its static analysis and explaining the design constraints. The mathematical proof for determining key design parameters is also given before being verified experimentally, together with other findings. The small-signal ac model of the converter is derived, and a type II compensator is designed to achieve closed-loop current control for LED dimming applications. A 200W PWM-resonant converter prototype was built to evaluate the converter performance under steady-state and transient conditions. Experimental and simulation results are provided to verify the theoretical analysis.**

Keywords **DC-DC power converters, resonant converters, zero-current switching, current control.**

I. INTRODUCTION

Countries around the globe are aiming to achieve “carbon neutrality” in the coming years to decrease the adverse impact of climate change resulting from the use of fossil fuels. There is an increase in demand for renewable energy sources to reduce the adverse effects of climate change. Renewable energy is clean and non-polluting to the environment. It is becoming crucial for power system applications like industrial, transportation, photovoltaic, etc.

In most of these applications, DC-DC converters, one type of power converter, are used [1]–[3]. Regarding the applications of DC-DC converters, DC-DC converters and resonant-type converters can be used in renewable energy systems. Renewable energy systems may require different types of energy conversion processes, such as DC-DC or DC-AC; therefore, research into efficient DC-DC converter topologies is an interesting topic.

In DC-DC converters, the DC input voltage is converted to a DC output voltage with a smaller or larger magnitude, possibly with reverse polarity. The converter capable of producing a smaller magnitude of the output voltage is known as a buck converter, and this traditional type of buck converter and its derivatives have been used in power electronics systems for the last several decades. A new type of step-down PWM-resonant converter has been proposed in [4] as a good alternative to the traditional buck converter with several advantages. The main arguments behind the emergence of this new type of step-down converter family are the following:

1) Smaller converter size,
2) Higher efficiency compared to traditional buck converters,
3) Maintaining fast transient response,
4) Good output voltage regulation capability.

The PWM-resonant converters can fulfill these desirable characteristics, so there is particular interest in these new converter topologies [4]–[6].

The conventional PWM converters operated in continuous conduction mode (CCM) were derived based on the prior-art buck converter, and the inductors employed by the converter must store DC energy in every switching cycle. As a direct consequence, a rapid response to any sudden load change is problematic due to the large value of passive components. The other critical point is that a boost (or buck) inductor is generally built with an air gap to prevent the saturation of the magnetic core since a high DC current flows through it. The effective inductance decreases with increasing air gap, which causes a noticeable increase in the inductor physical size [5]. The current trend in power electronics for achieving a smaller converter size and higher power density is to increase switching frequency using wide-bandgap semiconductors [7], [8]. However, increasing the switching frequency causes higher switching losses, which leads to efficiency issues. Because switching loss increases with the

Mustafa Gökdağ, is with Department of Electrical-Electronics Engineering, Industrial Electronics Lab (KBU-IEL), Karabuk University, Karabuk, Türkiye, (e-mail: mgokdag@karabuk.edu.tr). https://orcid.org/0000-0001-5589-2278

Ozan Gülbudak, is with Deparment of Electrical-Electronics Engineering, Industrial Electronics Lab (KBU-IEL), Karabuk University, Karabuk, Türkiye, (e-mail: ozangulbudak@karabuk.edu.tr). https://orcid.org/0000-0001-9517-3630

Uğur Ufuk Körpe, is with Deparment of Electrical-Electronics Engineering, Kırsehir Ahi Evran University, Kırsehir, Türkiye, (e-mail: ugur.korpe@ahievran.edu.tr). https://orcid.org/0000-0001-6450-1697

Manuscript received May 09, 2025; accepted Sep 14, 2025.
DOI: 10.17694/bajece.1696010

Copyright © BAJECE

switching frequency and imposes a maximum limit on the operating frequencies of practical converters. To overcome these shortcomings, the PWM-resonant converter recommends using a capacitive energy transfer approach. Using the resonance scaling technique, an inductor with a smaller inductance value can be used in converter design steps [4]–[6].

As mentioned, slow transient response, regardless of control methods, is a downside of the conventional PWM converters since many switching cycles must be passed through before the inductor reaches a new set point. In the case of load variations in resonant PWM-converters, the inductor current reaches a new reference value in a single switching cycle, which is a noticeable advantage over conventional PWM-converters [6]. In the power converter design approach, several selection criteria of power semiconductors, such as blocking voltage, on-resistance value, device output capacitance, etc., need to be considered. For instance, step-down PWM converters require switches with a blocking voltage higher than input voltage for a reliable conversion process. The input voltage of the buck-type converters is the highest voltage level during the whole converter operation. On the other hand, switches capable of blocking the output voltage are enough for PWM-resonant converters without regard to the system's input voltage. Thus, low-cost power semiconductors can be used in resonant versions of PWM converters. Besides, the dissipated power is expected to be degraded during switching transitions because the imposed voltage stress on the switches decreases [9], [10].

Switching mechanisms known as zero-current switching (ZCS) and zero-voltage switching (ZVS) are used for resonant converters. These techniques and resonant phenomena are also applied to conventional PWM converters to reduce switching losses at the expense of increased conduction losses [11]–[15].

In [9], a boost-type converter with a single switch and two diodes has been proposed, inspiring the PWM-resonant converter proposed by [4]. This converter employs two inductors; one operates as a conventional PWM inductor, and the other operates a resonant fashion. The inductor that operates in continuous conduction mode has DC current. Thus, an air gap is generally required to prevent saturation of the magnetic core. The main switch and diode operate in hard switching conditions, increasing the switching losses. The conversion ratios between 2-5:1 are possible. In [10], [16], a boost-type PWM-resonant converter that employs two resonant inductors has been proposed. This proposed converter emerged from inspiring the buck-type PWM-resonant converter reported in [4]. This new buck-type converter could find its origin in resonant switched-capacitor converters [10], [17]–[19] and has a continuously variable conversion ratio of 2:1. This allows the converter to operate over a wider range of operation points. A boosted version of a PWM-resonant converter can be easily derived by interchanging the input and output ports with proper manipulation of the circuit elements. It can be deduced that the conversion ratio of the boost-type PWM-resonant converter will be 1:2. In [16], a detailed static analysis of this topology, its operating principle, and a comprehensive analysis for power loss estimation have been presented. However, the derivation of the small-signal model of this converter family, compensator design steps for closed-loop implementation, and practical design aspects of selecting resonant parameters are still debatable. In , a boost-type PWM resonant converter is compared with a conventional CCM boost converter in terms of required inductor size, and dynamic response. However, experimental verification of the theoretical analyses and efficiency comparison between topologies have not been reported.

In this paper, the fundamentals of boost-type PWM-resonant converters are presented. A 200 W PWM-resonant boost converter prototype is built to validate all the theoretical analyses. The main contributions of this paper can be summarized as follows:

1) Static analysis and small-signal modeling: The static analysis of the converter is carried out for the PWM strategy with constant off-time and variable frequency. The duty cycle-to-output current small-signal transfer function is

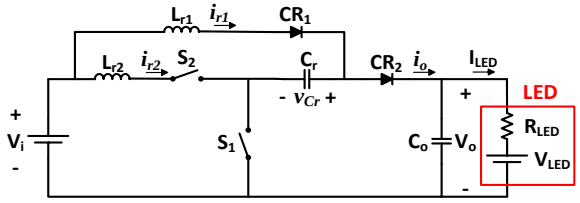


Fig. 1. Boost-type PWM-resonant converter

derived to reveal the converter`s dynamic characteristics for possible current dimming applications. Using the state-space averaged modeling method, the dominant behavior of the PWM-resonant converter is understood while forsaking other insignificant phenomena. A selection procedure for resonant components is presented.

2) Closed-loop performance evaluation: The designed control loop is tested experimentally to assess the linear controller's reference tracking capability during rapid load changes.

The outline of the paper is as follows. Section 2 describes the comprehensive static analyses of the PWM-resonant boost converter and converter design constraints. Section 3 presents the small-signal modeling of the converter and the derivation of the control-to-output current transfer function. Moreover, type-II controller design steps are explained. Section 4 presents simulation results, and Section 5 presents the experimental results. Lastly, Section 6 is the conclusion part of the paper.

II. FUNDAMENTALS OF BOOST-TYPE PWM-RESONANT CONVERTER

A. Operating Principle

The boost-type PWM-resonant converter topology is shown in Figure 1, where an LED bulb is connected to the output port of the converter as a load. The LED bulb is

modeled using the constant voltage V_{LED} model plus a series-connected resistor R_{LED}. Two resonant inductors $L_{r1\text{-}2}$, and one resonant capacitor C_r are used in the circuit to transfer the power in a resonant fashion and obtain zero-current switching. An output capacitor C_o is used to filter the output voltage V_o. Two active switches and two diodes block voltages and currents properly. The PWM strategy with constant off-time under variable switching frequency is applied to the converter [4]. Figure 2 shows associated resonant currents in each switching state of the circuit. In this PWM strategy, the on- and off-time intervals are allocated over the switching period according to the ratio between resonant inductor values, as presented in Equation (1), where the duty cycle is restricted to D≤0.5.

According to Equation (1), the ratio between resonant inductors is defined as $m^{2,}$ and the selection of the m is a crucial design step for the PWM resonant converter.

$$\begin{gathered} L_{r1} = m^2 L_{r2} \\ T_{SW} = T_{ON} + T_{OFF} = DT_{r1} + 0.5T_{r2} \\ T_{SW} = D2\pi\sqrt{L_{r1}C_r} + \pi\sqrt{L_{r2}C_r}, \quad T_{SW_MAX} \ for\ D = 0.5 \\ T_{SW} = Dm2\pi\sqrt{L_{r2}C_r} + \pi\sqrt{L_{r2}C_r} \\ T_{SW} = \pi\sqrt{L_{r2}C_r}(1 + 2mD) \\ T_{SW} = {}^{T_{r2}}/_{2}\,(1 + 2mD) \\ T_{SW} = {}^{T_{r1}}/_{2m}\,(1 + 2mD) \end{gathered} \tag{1}$$

The related resonant current loops for each switching time interval are shown in Figure 3, and the operation of the converter for these intervals is as follows [16].

Interval t_0-t_1: This time interval is initialized by turning on the switch S_1, and the resonant circuit shown in Figure 3(a) is formed. The resonant current i_{r1} is drawn from the supply and charges the resonant capacitor C_r. It should be noted that the resonant current i_{r1} completes its half-cycle if the duty cycle D=0.5. During this interval, the zero current switching is always guaranteed at the turn-on transitions of S_1 and C_{R1}, while the zero current switching for the turn-off transition of S_1 is accomplished only for D=0.5.

Interval t_1-t_3: This time interval appears for the case where the duty cycle D for the switch S_1 is less than 0.5. In this case, the resonant inductor current i_{r1} is interrupted due to the S_1 turn-off. This current interruption of the inductor L_{r1} forward biases the diodes C_{R1} and C_{R2}, and the circuit shown in Figure 3(b) is formed. Thus, the inductor current linearly decays to zero through the interval D_2T_S, which is the freewheeling period for the inductor L_{r1}. This linearly decaying current charges the output capacitor. At the end of this interval, the rectifier diode C_{R1} turns off with zero current switching.

Interval t_2-t_4: This time interval is initialized by turning on the switch S_2, which consequently forward biases the C_{R2}. Thus, the resonant circuit is formed between L_{r2} and C_r, as shown in Figure 3(b) and (c), and the resonant current i_{r2} flows from the input to the converter's output. This resonant current always completes its half-cycle since the off-time interval T_{OFF} equals half of the resonant period T_{r2} as defined by Equation (1). According to this operation principle, the zero-current turn-on and turn-off for S_2 and the zero-current turn-off for C_{R2} are always attained.

B. Converter Static Analysis

According to the current waveforms shown in Figure 2, the resonant inductor L_{r1} is volt-second balanced during the time interval t_0-t_3, while the resonant inductor L_{r2} is volt-second balanced during the interval t_2-t_4. Thus, the volt-second balance expression for L_{r1} yields Equation (2).

$$D_2(V_i - V_o) + \frac{mR_{N1}I_{m1}}{\pi(1 + 2mD)} sin(2\pi D) = 0, \quad 0 < D \le 0.5 \tag{2}$$

where R_{N1} is the characteristic impedance of the resonant tank L_{r1}-C_r during the time interval t_0-t_1 and given by Equation (3). The characteristic impedance R_{N2} of the resonant tank L_{r2}-C_r during the time interval t_2-t_4 can also be defined as in Equation (3). The quality factor Q for the PWM-resonant converter can be defined in Equation (4) for use in various analyses.

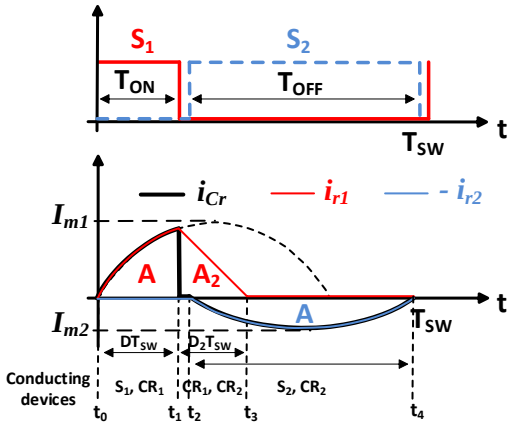


Fig. 2. Switching state diagram with variable frequency and constant off-time (top), and related resonant currents (bottom)

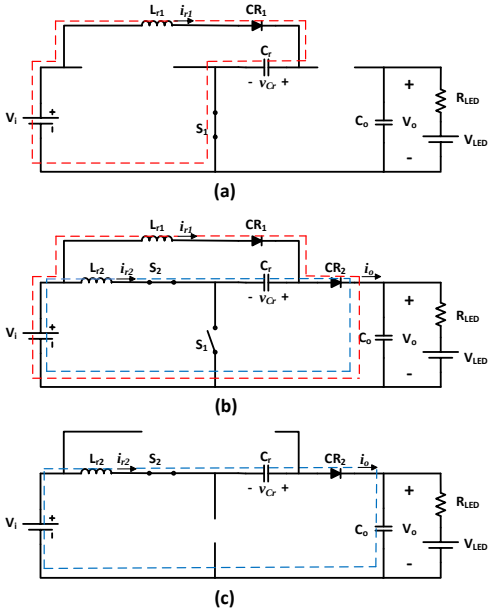


Fig. 3. Resonant converter with corresponding current loops

$$R_{N1} = \sqrt{L_{r1}/C_r}$$
$$R_{N2} = \sqrt{L_{r2}/C_r} \quad (3)$$
$$R_{N1} = mR_{N2}$$
$$Q = R_{N1}/R_{eff} \quad (4)$$

The resonant currents i_{r1} and i_{r2} flow in opposite directions through the resonant capacitor C_r, and the charge balance requirement is fulfilled. By equating the A areas under the resonant current waveforms shown in Figure 2, Equation (5) can be written for the relationship between the magnitudes of the resonant currents i_{r1} and i_{r2}.

$$I_{m1} = \frac{2I_{m2}}{m\left(1-cos(2\pi D)\right)} \qquad 0 < D \leq 0.5 \quad (5)$$

The average load current, also equal to the average resonant inductor L_{r1} current, is obtained as in Equation (6).

$$I_{LED} = I_{Lr1} = \frac{mI_{m1}}{\pi(1+2mD)}\left(1-cos(2\pi D)\right) + \frac{D_2 I_{m1}}{2} sin(2\pi D) \quad (6)$$

Equating the input and output powers for an ideal lossless converter, the magnitude of resonant inductor current I_{m1} is obtained as in Equation (7) regarding the input and output voltages, load current, and other circuit parameters.

$$I_{m1} = \frac{I_{\text{LED}}(V_o - V_i)}{V_i} \frac{\pi(1+2mD)}{m\left(1-cos(2\pi D)\right)} \quad (7)$$

The voltage conversion ratio of the converter can be written as in Equation (8) by substituting Equation (7) into Equation (6). The load current can also be expressed as in Equation (9) by substituting Equation (7) into Equation (2).

$$\frac{V_o}{V_i} = \frac{2\,tan(\pi D) + \left(\frac{\pi(1+2mD)}{2m} D_2\right)}{tan(\pi D) + \left(\frac{\pi(1+2mD)}{2m} D_2\right)} \quad (8)$$

$$I_{\text{LED}} = \frac{V_i D_2}{R_{N1}} tan(\pi D) \qquad only\ valid\ for\ D_2 > 0 \quad (9)$$

Equation (10) can be easily written to express the relationship between output voltage and load current.

$$V_o = V_{\text{LED}} + R_{\text{LED}} I_{\text{LED}} \quad (10)$$

According to Equation (8), the voltage conversion ratio equals 2 when the converter operates with D=0.5, and the conversion ratio varies from 1-to-2 for duty cycle values between 0 and 0.5.

C. Design Constraints

Using Equations (1)-(8), a family of conversion ratio curves versus duty cycle D and the switching frequency f_{sw}, as shown in Figure 4 and Figure 5, can be plotted for different quality factor values. It can be deduced from Figure 4 that the conversion ratio curves have approximately linear behavior for quality factor Q values between 0.08 and 0.24. The region where linear conversion ratio curves are obtained is vital for a safe operation. The conversion ratio curves plotted for Q=0.08-0.24 impose a fundamental design limitation for the selection of resonant components. The expression (11), which is derived from Equation (4), can be used to select the values of resonant components.

$$L_{r1} = \frac{mQR_{eff}}{\pi(1+m)f_{sw_MIN}}$$
$$C_r = \left(\frac{m}{\pi(1+m)f_{sw_MIN}}\right)^2 \frac{1}{L_{r1}} \quad (11)$$

where R_{eff} is the effective load resistance and is calculated by V_o/I_{load}.

In the design of the PWM-resonant converter, the current ability to share between the resonant inductors can be adjusted by selecting the m factor. To control the voltage conversion ratio over a relatively wide range of duty cycle D, m≥1 is a desired selection criterion. The peak and rms values of the resonant inductor current i_{r2} increase sharply for m>4. This results in increased conduction losses and causes EMI problems. Therefore, selecting m between 1 and 4 is a reasonable design consideration.

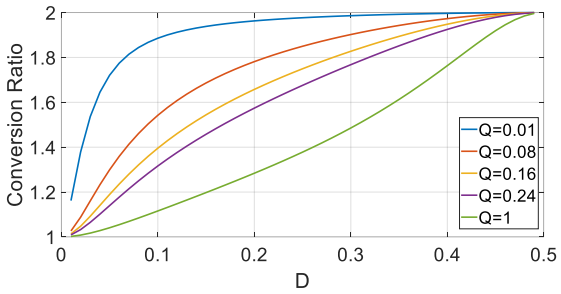


Fig. 4. Conversion ratio versus duty cycle D with the different values of quality factor (V_i=60 V, R=50 Ω, m=3.8452)

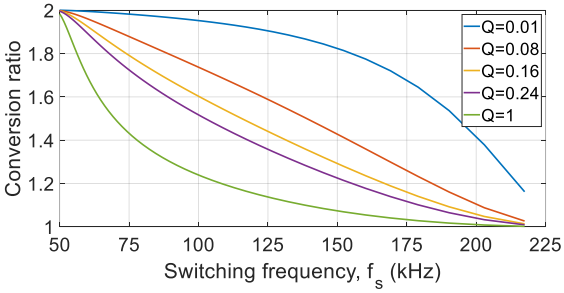


Fig. 5. Conversion ratio versus switching frequency f_{sw} with the different values of quality factor (V_i=60 V, R=50 Ω, m=3.8452)

III. SMALL SIGNAL MODELLING AND COMPENSATOR DESIGN

A. Small Signal Modelling of PWM-Resonant Converter

The control-to-output transfer function is required to accomplish the closed-loop control of the PWM-resonant converter. The state-space averaged model is necessary to derive the small-signal transfer functions of a switching converter [20], [21]. The system order for a converter operating in CCM is defined by the total number of energy storage components, e.g., capacitors and inductors. However, it must be considered that the inductor current has no free boundaries for a converter operating in DCM. Therefore, the DCM inductor current is not considered a state variable, and the system order is lowered by one [22], [23]. The DCM inductor L_{r1} is ignored in the state-space model. The other two resonant components, L_{r2} and C_r, are responsible for transferring the energy in a resonant manner, and the dynamic effect caused by these components is much faster than the converter's overall natural frequency. Thus, they are also neglected in the state-space model for simplicity since the dominant pole, caused by the output capacitor C_o, already attenuates the high-frequency dynamics of the resonant components.

According to the above explanation, the state-space averaged model of the converter can be expressed as a first-order model due to the output capacitor C_o.

$$C_o\frac{dv_o}{dt} = -\frac{v_o - V_{LED}}{R_{LED}} + \frac{mi_{m1}}{\pi(1+2md)}\left(1-cos(2\pi d)\right) + \frac{d_2 i_{m1}}{2}sin(2\pi d) \tag{12}$$

After applying perturbation and linearization steps to Equation (12), the dynamic model of the output capacitor is obtained as in Equation (13).

$$sC_o\widetilde{v_o}A = -\frac{A\widetilde{v_o}}{R_{LED}} + \tilde{d}K + \widetilde{\imath_{m1}}M + \widetilde{d_2}N \tag{13}$$

The modulation quantities $\widetilde{\imath_{m1}}$ and $\widetilde{d_2}$ must be expressed as functions of $\widetilde{v_o}$ and $\tilde{d}$, and they can be obtained from Equation (2) and Equation (8), respectively, after applying the usual perturbation and linearization steps. These modulation quantities and all other quantities denoted by capital letters in the small-signal modelling are reported in the appendix.

The first-order dynamic model from control to output can be expressed by Equation (14).

$$G_{vd}(s) = \frac{\widetilde{v_o}}{\tilde{d}}(s) = \frac{Y}{sAC_o + B} \tag{14}$$

Suppose the output voltage is desired to be controlled for a resistive load case. In that case, the equivalent LED resistance R_{LED} in the relevant equations is replaced with the load resistance R, and Equation (14) is used in the compensator design. In an LED driver application, the LED current, which is the load current of the converter, is the control variable. In this case, Equation (14) is updated as in Equation (15) using the relationship of $\widetilde{\imath_{LED}} = \widetilde{v_o}/R_{LED}$ to design the compensator.

$$G_{id}(s) = \frac{\widetilde{\imath_{LED}}}{\tilde{d}}(s) = \frac{Y/R_{LED}}{sAC_o + B} \tag{15}$$

B. Compensator Design

To properly design the compensator for the control-to-output current transfer function given in Equation (15), its frequency response is plotted using the parameters in Table 1 and displayed in Figure 6(a). According to the Bode plot, a type-II compensator given in Equation (16) is sufficient to shape the loop function to achieve a smooth response without oscillation. The origin pole of the type-II compensator provides the required low-frequency gain to accomplish zero steady-state error, whereas the zero frequency maintains the phase margin, and lastly, the high-frequency pole is employed to roll off the gain.

In agreement with the above explanation, the crossover frequency of the loop function is located at 1.92 kHz and the phase margin is set to 79º. The frequency response of the compensated loop function is shown in Figure 6(b).

$$G_c(s) = G_{m_ci}\frac{1+\frac{\omega_{z_ci}}{s}}{\left(1+\frac{s}{\omega_{p_ci}}\right)} = \left(G_{m_ci}\omega_{z_ci}\right)\frac{1+\frac{s}{\omega_{z_ci}}}{s\left(1+\frac{s}{\omega_{p_ci}}\right)} \tag{16}$$

where $G_{m_ci} = 0.0862$ $f_{z_ci} = 1.2$ kHz and $f_{p_ci} = 10$ kHz for closed-loop current control of the LED dimming application (the bandwidth is 1.92 kHz), and $G_{m_ci} = 0.1094$, $f_{z_ci} = 0.8$ kHz and $f_{p_ci} = 18$ kHz for closed-loop output voltage control in case of resistive load (the bandwidth is 5 kHz). To apply the compensator in digital platforms, it is discretized using the Tustin bilinear mapping technique, and its discrete form is given in Equation (17).

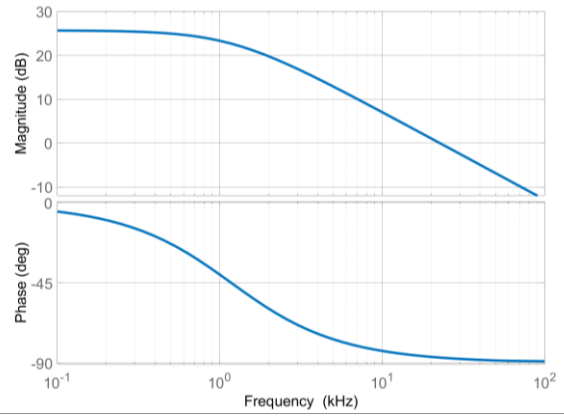
$$\begin{aligned} d(k) = d(k-1)\,&\frac{8}{2\omega_{p_ci}T_s+4} + d(k-2)\,\frac{2\omega_{p_ci}T_s-4}{2\omega_{p_ci}T_s+4} \\ &+ e_i(k)\,\frac{G_{m_ci}\omega_{p_ci}T_s\left(\omega_{z_ci}T_s+2\right)}{2\omega_{p_ci}T_s+4} \\ &+ e_i(k-1)\,\frac{2G_{m_ci}\omega_{p_ci}\omega_{z_ci}T_s^2}{2\omega_{p_ci}T_s+4} \\ &+ e_i(k-2)\,\frac{G_{m_ci}\omega_{p_ci}T_s\left(\omega_{z_ci}T_s-2\right)}{2\omega_{p_ci}T_s+4} \end{aligned} \tag{17}$$

where the sampling frequency for digital implementation was chosen as 25 kHz, which is sufficient for a 2-5 kHz bandwidth closed-loop system, d is the output of the compensator, and e is the error signal. The control schematic is illustrated in Figure 7.

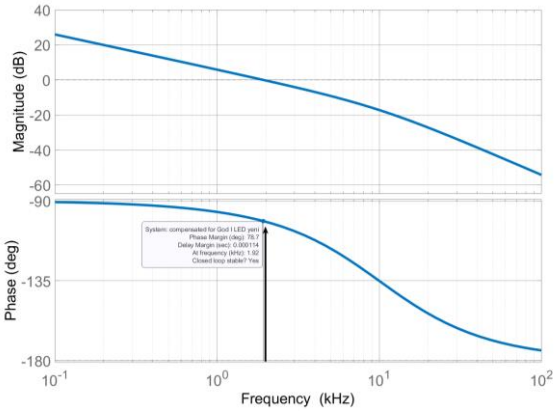
Table 1
Parameters for the operating point and values for passive components

Parameters	Value
Input voltage, V_i	60 V

Output voltage, V_o	100.4 V
Amplitude of I_{m1}	6.26 A
Amplitude of I_{m2}	4.54 A
Duty cycle, D	0.143
D_2	0.271
Load resistance, R	50 Ω
Inductor, L_{r1}	20.7 µH
Inductor, L_{r2}	1.4 µH
m	3.8452
Output capacitor, C	88 µF
Resonant capacitor, C_r	1.32 µF
Switching freq., f_{sw}	111.52 kHz
LED voltage V_{LED}	96 V
LED resistance R_{LED}	2 Ω



(a)



(b)

Fig. 6. Frequency responses: (a) for control to output current transfer function $G_{id}(s)$, (b) for compensated loop function $T(s) = G_{id}(s) * G_c(s)$.

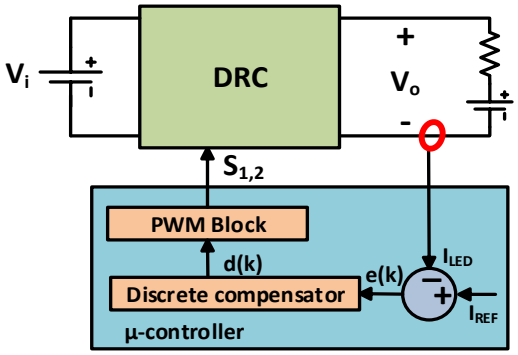


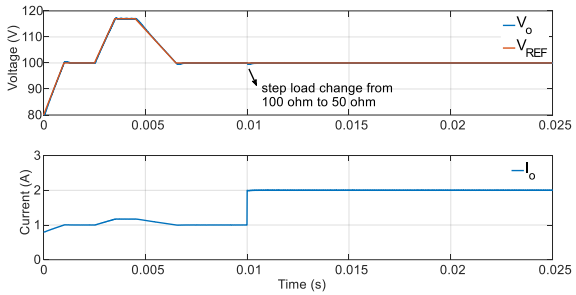
Fig. 7. Control schematic

IV. SIMULATION RESULTS

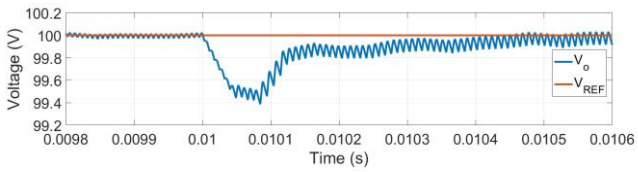
Simulation results for the PWM resonant converter are presented in this section. The system depicted in Figure 7 is built in the simulation, and the converter is simulated with the parameters listed in Table 1. The digital controller with a sampling frequency of 25 kHz is implemented in the simulation.

A. Closed-Loop Control of Load Voltage

The converter's output voltage reference tracking ability is first tested for a resistive load case. A reference output voltage with the pattern shown in Figure 8(a) is applied to the closed-loop controlled converter. As shown in Figure 8(a), the output voltage tracks the reference in a wide range between 80-117 V. A step-up load change (100Ω→50Ω) at t=0.01s is also applied, and the zoomed-in version of the dynamic response is presented in Figure 8(b). After the step input, an undershoot of around 0.6%, which is quite acceptable, is observed, and the system settles down to the reference value.



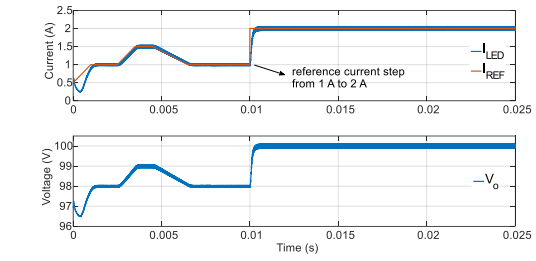
(a)



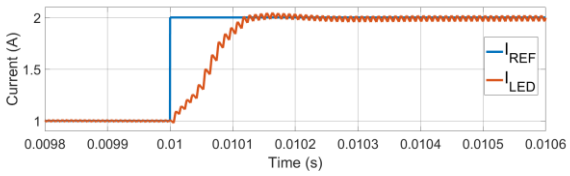
(b)

Fig. 8. (a) Dynamic response of the output voltage for the closed-loop controlled PWM-resonant boost converter, (b)

zoom-in version of the load step transition from 100 Ω to 50 Ω.



(a)



(b)

Fig. 9. (a) Dynamic response of the output current, (b) zoom-in version of the load current response to a step change from 1 A to 2 A.

B. Closed-Loop Control of Load Current

The converter's closed-loop output current control ability is tested for LED dimming applications. For this purpose, the reference for the output current is varied in a pre-defined pattern, as shown in Figure 9(a). The output current follows the reference well. A step change from 1 A to 2 A is applied to output the current reference, and the converter gives a quick response with a smooth transition, as observed in Figure 9(b).

V. EXPERIMENTAL RESULTS

All theoretical analysis for the PWM-resonant converter is verified on a 200W lab-scale prototype shown in Figure 10, which highlights the various components and sub-circuits, such as the energy storage components and the gate driver circuitry. The experimental test bench is also shown in Figure 11. The F28379D LaunchPad™ development kit implements the closed-loop control from sensing the voltages/currents to generating PWM signals.

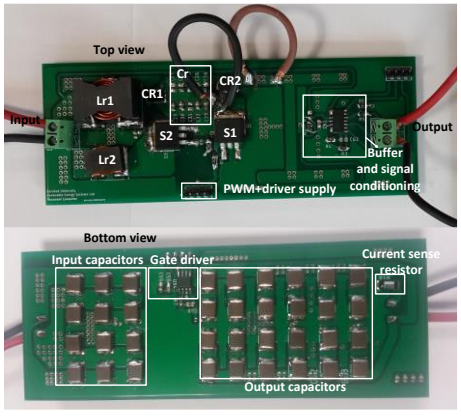


Fig. 10. Close-up picture of 200W PWM-resonant converter

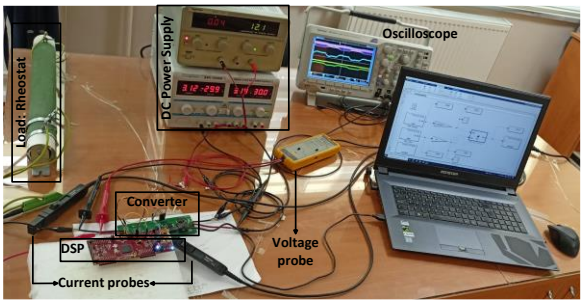


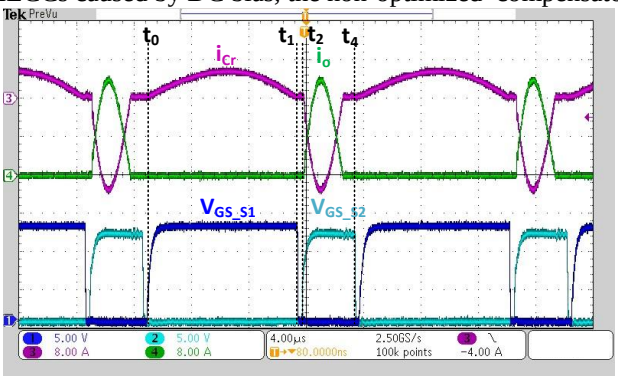
Fig. 11. Experimental test bench

The experimental current waveforms and corresponding gate signals are presented in Figure 12(a) for the case where the converter is operated with D=0.5 and a load resistance of 50 Ω. This experiment converts 60 V input voltage to 117 V output voltage, which agrees with the expected voltage conversion ratio of 1-to-2 for D=0.5. The channel III waveform in Figure 12(a) presents the resonant capacitor current i_{Cr} measurement, and its positive portion belongs to the resonant inductor current i_{r1}. In contrast, the negative portion is the resonant inductor current i_{r2}. As Figure 12(a) shows, the resonant current i_{r1} completes its half-cycle for D=0.5, and all switches and diodes of the converter operate with zero-current switching. In order to make the ZCS intants more obvious, dashed auxiliary lines have been added to Figure 12, and these time instants have been labeled as t_0–t_4, consistent with those in Figure 2. The experimental results in Figure 12 are in agreement with the operating principle described under Section II-A.

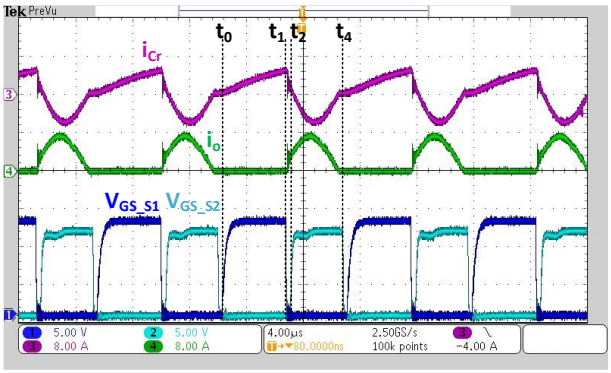
The experimental current waveforms for the converter operated with D<0.5 to obtain the variable conversion ratios ranging between 1 and 2 are presented in Figure 12(b). In this experiment, a 60 V input voltage is converted to a 100 V output voltage, and the converter is controlled with a PWM technique where constant off-time variable on-time under varying switching frequency is used. As shown in Figure 12(b), the resonant inductor current i_{r1}, the positive portion of the resonant capacitor current i_{Cr}, does not complete its half-cycle. The effect of the linearly decaying portion of the i_{r1} can be observed from the rectifier diode CR_2 current i_o, which does not start from zero.

The converter is operated under closed-loop control, and output voltage and current regulation capabilities are evaluated. The discrete-time version of the Type II compensator (17) is implemented using TMS320F28379D, and the sampling period T_S is set to 40 µs. First, the output voltage regulation of the closed-loop controlled converter is tested for a step change in load resistance. The load step from 100 Ω to 50 Ω is applied to the closed-loop system when the input voltage V_i = 60 V and the output voltage V_o = 100 V (see Figure 13(a)). In this case, the load current jumps from 1 A to 2 A; see Figure 13(a) (Channel 4), and an opposite reaction occurs in the output load voltage (Channel 2). As presented in Figure 13(a), the undershoot in output voltage is kept at less than 7% and returns to regulation at around 4 ms while a new set point for the load current is achieved. During this load transition, the controller adjusts the PWM signals appropriately to track the new reference trajectory. The difference between simulation and experimental output voltage undershoot value under step load change is mainly

due to the significant reduction of effective capacitance in MLCCs caused by DC bias, the non-optimized compensator design for actual component values, and the non-negligible ESR of real capacitors, which was not modeled in the simulations. The output voltage reference is also periodically varied as a step function between 90 V and 100 V to observe the closed-loop response. As shown in Figure 13(b), the reference trajectory for the output voltage is quite good. The output current regulation is also tested for possible LED dimming applications. For this purpose, an LED bulb (V_{LED}=93V @ 2A) is connected to the output port of the converter. A step change from 1.7A to 2A is periodically applied to the output current reference. The output current quickly responds to step variations, as shown in Figure 13(c).



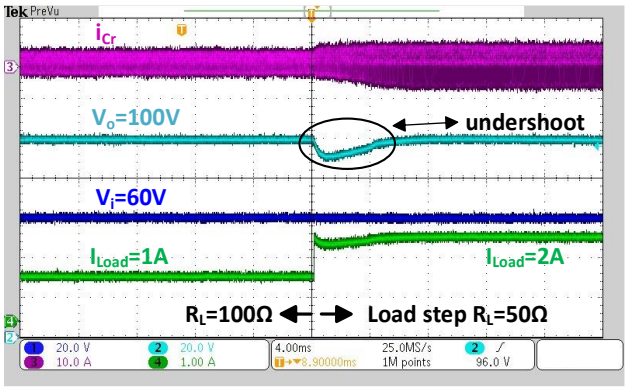
(a)



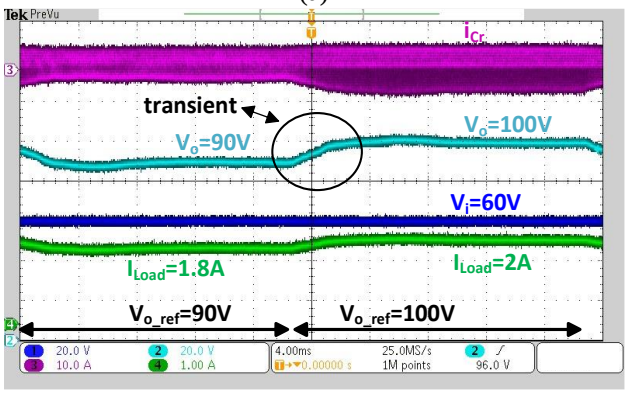
(b)

Fig. 12. Current waveforms: (a) is for the case of fixed conversion ratio (1-to-2) where V_o=117 V, V_i=60 V, R=50 Ω, f_{sw}=68 kHz, (b) for the case of variable conversion ratio (1-to-1.67) where V_o=100 V, V_i=60 V, R=50 Ω, f_{sw}=113 kHz. Resonant capacitor current i_{Cr} (channel 3, 8A/div), rectifier diode C_{R2} current i_o (channel 4, 8A/div), gate signal for S_1 (channel 1, 5V/div), gate signal for S_2 (channel 2, 5V/div) from top to bottom.

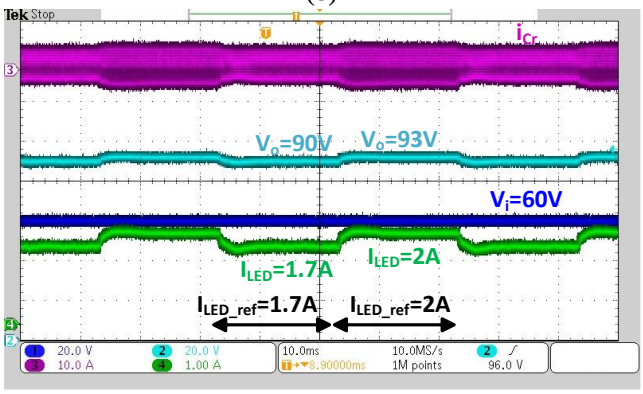
The converter efficiency curve for varying input power levels is plotted in Figure 14. In the efficiency measurement, the input and output voltages are V_i=60 V and V_o=100 V. The load resistance varies from 250 Ω to 50 Ω with 50 Ω steps. The closed-loop compensator ensures the constant output voltage under varying loading conditions. The switching frequency is automatically adjusted between 113-175 kHz by the controller to fix the output voltage at 100 V. According to the efficiency curve presented in Figure 14, the efficiency remains above 97% for a wide range of input power levels, and the curve exhibits a peak efficiency of 97.4 at 200W which is the design point of the converter. In power efficiency measurement, input/output currents are measured with the Brymen BM867 multimeter and input/output voltage is measured with the Fluke 175 multimeter.



(a)



(b)



(c)

Fig. 13. The output voltage dynamic responses: (a) is for the step change in load resistance from 100 Ω to 50 Ω, V_i = 60 V and V_o = 100 V, (b) is for the step change in load voltage reference from 90 V to 100 V or vice versa, V_i = 60 V and R = 50 Ω. Resonant capacitor current i_{Cr} (channel 3), output voltage V_o (channel 2, 20 V/div), input voltage V_{in} (channel 1, 20 V/div), load current (channel 4, 1 A/div) from top to bottom.

For a performance comparison with previously reported work, reference [10] can be considered. In [10], a 120 W resonant switched-capacitor step-up converter operating from a 48 V input and capable of delivering output voltages in the range of 62 V to 94.6 V is presented. The prototype achieves a maximum efficiency of 95.5% at an output voltage of 86 V and an output current of 1.1 A. In [24], the converter topology

presented in [10] is slightly modified to incorporate a passive regenerative snubber, enhancing energy recovery during switching transitions. A 125 W resonant switched-capacitor converter prototype is implemented, operating from a 50 V input and capable of delivering output voltages in the range of 66 V to 99.25 V. The prototype achieves an overall efficiency of 95.7% at an output voltage of 80 V and an output current of 1.25 A. When operated with a boosting ratio of 2,

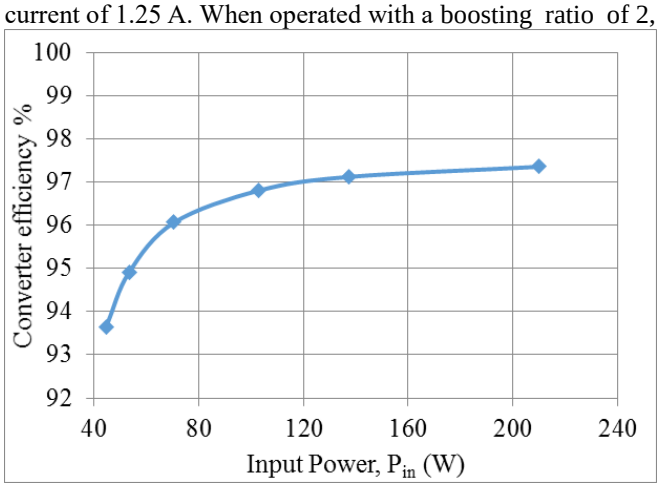


Fig. 14. Converter efficiency curve for varying power levels

the converter demonstrates an efficiency of 96.8% at an output power of 116 W.

VI. CONCLUSION

This study proposes a boost-type PWM-resonant converter, which can be considered an alternative to classical PWM converters for LED dimming applications. The static analysis of the boost-type PWM-resonant converter is presented by explaining its fundamental power conversion principle. The control-to-output current small-signal model is derived, and the dynamic characteristics of this new type of converter are revealed. Type II compensator is designed for closed-loop implementation, and the performance of the PWM-resonant boost converter combined with a linear controller is experimentally evaluated. All proposed mathematical models are verified using a 200 W lab-scale prototype. As reported by the experimental results, the PWM-resonant boost converter has a peak efficiency of 97.4%.

REFERENCES

[1] S. Kumar, S. Kumar, S. Singh, and A. Das, "Design and development of variable frequency modulation-based isolated DC–DC converter with green mode of operation," *Electr. Eng.*, 2024, doi: 10.1007/s00202-024-02315-w.

[2] X. J. Zhou and Y. R. Huang, "Structure evolving and comparative analysis of grid-connected converter output filter," *Electr. Eng.*, vol. 105, no. 3, pp. 1849–1865, 2023, doi: 10.1007/s00202-023-01780-z.

[3] X. Ding, C. Zhang, K. Jiang, W. Dai, and P. Zhang, "A class of Sepic-based DC-DC converters with improved voltage multiplier cell," *Electr. Eng.*, vol. 107, no. 6, pp. 6997–7010, 2024, doi: 10.1007/s00202-024-02908-5.

[4] S. Cuk and L. Niguel, "Four-switch step-down storageless converter," US 8,134,351 B2, 2012.

[5] S. Ćuk, "New topology eliminates magnetic cores at 50 kHz NOT 50MHz!," 2017, doi: 10.1109/GECS.2017.8066120.

[6] S. Cuk, "Step-Down dc-dc Converter Eliminates Ferrite Cores at 50kHz Enabling Power Supply on Chip with One-Cycle Transient," *Power Electronics*, 2017. .

[7] M. Fu, C. Fei, Y. Yang, Q. Li, and F. C. Lee, "A two-stage rail grade DC/DC converter based on GaN device," in *Conference Proceedings - IEEE Applied Power Electronics Conference and Exposition - APEC*, 2019, pp. 2110–2114, doi: 10.1109/APEC.2019.8722095.

[8] Y. Cai, M. H. Ahmed, Q. Li, and F. C. Lee, "Optimized design of integrated PCB-winding transformer for MHz LLC converter," in *Conference Proceedings - IEEE Applied Power Electronics Conference and Exposition - APEC*, 2019, pp. 1452–1458, doi: 10.1109/APEC.2019.8722181.

[9] A. Ciresan, S. Lica, D. Lascu, and M. Tomoroga, "A novel low-stress high-efficiency step-up DC-DC converter," in *2015 19th International Conference on System Theory, Control and Computing, ICSTCC 2015 - Joint Conference SINTES 19, SACCS 15, SIMSIS 19*, 2015, pp. 830–835, doi: 10.1109/ICSTCC.2015.7321397.

[10] S. Li, Y. Zheng, and K. M. Smedley, "A Family of Step-Up Resonant Switched-Capacitor Converter with a Continuously Adjustable Conversion Ratio," *IEEE Trans. Power Electron.*, vol. 34, no. 1, pp. 378–390, 2019, doi: 10.1109/TPEL.2018.2812198.

[11] G. Yao, A. Chen, and X. He, "Soft Switching Circuit for Interleaved Boost Converters," *IEEE Trans. Power Electron.*, vol. 22, no. 1, pp. 73–115, 2007, doi: 10.1109/TPEL.2006.886649.

[12] S. Fan, L. Sun, and K. Zhang, "Improved active clamped ZVS buck converter with freewheeling current transfer circuit," *IET Power Electron.*, vol. 12, no. 6, pp. 1341–1348, 2019.

[13] R. W. Erickson and D. Maksimovic, *Fundamentals of Power Electronics*. New York, NY, USA: Kluwer, 2004.

[14] K. A, A. Bhattacharya, and P. K. Sadhu, "Design and analysis of a single-stage three-leg resonant converter with PFM-ADC control," *Electr. Eng.*, vol. 107, no. 2, pp. 2257–2271, 2025, doi: 10.1007/s00202-024-02632-0.

[15] D. Ma and J. Jiang, "A current source inverter with zero-voltage-switching for low-input voltage PMSM drive application," *Electr. Eng.*, vol. 105, no. 5, pp. 3161–3173, 2023, doi: 10.1007/s00202-023-01861-z.

[16] M. Gokdag, "Comparison of Boost-Type Ćuk's Pwm-Resonant Converter With Conventional Boost Converter," in *2018 2nd International Symposium on Multidisciplinary Studies and Innovative Technologies (ISMSIT)*, 2018, pp. 1–4.

[17] S. Li, W. Xie, and K. M. Smedley, "A Family of an Automatic Interleaved Dickson Switched-Capacitor Converter and Its ZVS Resonant Configuration," *IEEE Trans. Ind. Electron.*, vol. 66, no. 1, pp. 255–264, 2019, doi: 10.1109/TIE.2018.2829682.

[18] S. Li, N. Zhang, S. Zheng, W. Xie, and K. Smedley, "A dickson resonant switched-capacitor converter with indirect resonant core and continuous conversion ratio," in *Conference Proceedings - IEEE Applied Power Electronics Conference and Exposition - APEC*, 2019, pp. 2218–2222, doi: 10.1109/APEC.2019.8721994.

[19] S. Li, S. Liang, S. Zheng, W. Xie, and K. Smedley, "A cuk dual resonance core based dickson resonant switched-capacitor converter with wide conversion ratio range," in *Conference Proceedings - IEEE Applied Power Electronics Conference and Exposition - APEC*, 2019, pp. 2274–2278, doi: 10.1109/APEC.2019.8722242.

[20] S. Ćuk and R. Middlebrook, "A general unified approach

to modelling switching DC-to-DC converters in discontinuous conduction mode," in *PESC Record - IEEE Annual Power Electronics Specialists Conference*, 1977, pp. 36–57, doi: 10.1109/PESC.1977.7070802.

[21] D. Maksimovic and S. Cuk, "A unified analysis of PWM converters in discontinuous modes," *IEEE Trans. Power Electron.*, vol. 6, no. 3, pp. 476–490, 1991, doi: 10.1109/63.85890.

[22] S. Nigsch, S. Cuk, and K. Schenk, "Analysis, modeling and design of a True Bridgeless Single Stage PFC with galvanic isolation," in *Conference Proceedings - IEEE Applied Power Electronics Conference and Exposition - APEC*, 2015, pp. 469–476, doi: 10.1109/APEC.2015.7104392.

[23] S. Cuk, "Modelling, Analysis, and Design of Switching Converters," Caltech, 1977.

[24] W. Xie, S. Li, K. M. Smedley, J. Wang, Y. Ji, and J. Yu, "A Family of Dual Resonant Switched-Capacitor Converter with Passive Regenerative Snubber," *IEEE Trans. Power Electron.*, vol. 35, no. 5, pp. 4891–4904, 2020, doi: 10.1109/TPEL.2019.2945796.

APPENDIX

$$A = \pi(1 + 2mD) \tag{A1}$$

$$K = mI_{m1}2\pi sin(2\pi D) + \pi mI_{m1}D_2 sin(2\pi D) + \pi AD_2 I_{m1} cos(2\pi D) - 2\pi mI_{\text{Load}} \tag{A2}$$

$$M = m\big(1 - cos(2\pi D)\big) + 0.5AD_2 sin(2\pi D) \tag{A3}$$

$$N = 0.5AI_{m1} sin(2\pi D) \tag{A4}$$

$$\widetilde{\iota_{m1}} = \frac{\tilde{d}\big(2\pi mD_2(V_o - V_i) - 2\pi mR_{N1}I_{m1}cos(2\pi D)\big)}{mR_{N1}sin(2\pi D)} + \frac{\widetilde{d_2}\big(A(V_o - V_i)\big)}{mR_{N1}sin(2\pi D)} + \frac{\tilde{v}AD_2}{mR_{N1}sin(2\pi D)} \tag{A5}$$

$$\widetilde{d_2} = \frac{\tilde{d}\left(2\pi m(2V_i - V_o) - (V_o - V_i)\big(2\pi mD_2 - \pi AD_2 tan(\pi D)\big)\right)}{A(V_o - V_i)} + \frac{\tilde{v}(-2mtan(\pi D) - AD_2)}{A(V_o - V_i)} \tag{A6}$$

$$B = +\frac{A}{R_{LED}} - \frac{MD_2A}{mR_{N1}sin(2\pi D)} + \frac{P(2mtan(\pi D) + AD_2)}{A(V_o - V_i)} \tag{A7}$$

$$Y = K + \frac{M\big(2\pi mD_2(V_o - V_i) - 2\pi mR_{N1}I_{m1}cos(2\pi D)\big)}{mR_{N1}sin(2\pi D)} + \frac{P\big(2\pi m(2V_i - V_o) + (V_o - V_i)(\pi AD_2 tan(\pi D) - 2\pi mD_2)\big)}{A(V_o - V_i)} \tag{A8}$$

$$P = N + \frac{MA(V_o - V_i)}{mR_{N1}sin(2\pi D)} \tag{A9}$$

BIOGRAPHIES



Mustafa Gokdag received his B.Sc. degree with honors in Electrical and Electronics Engineering from Fırat University, Türkiye, in 2009. He obtained his M.Sc. and Ph.D. degrees in Electrical and Electronics Engineering from Karabuk University, Türkiye, in 2011 and 2016, respectively. From 2009 to 2016, he served as a Research Assistant in the Department of Electrical and Electronics Engineering at Karabuk University. He was appointed as an Assistant Professor in 2016 and promoted to Associate Professor in 2023 in the same department. His research interests include the modeling and control of DC-DC power converters, as well as model predictive control (MPC) of AC-DC, DC-AC, and AC-AC power converters, particularly for renewable energy systems and electric drive applications.



Ozan Gulbudak received the Ph.D. degree in electrical engineering from the University of South Carolina, Columbia, SC, USA, in 2016. He is a faculty member in Department of Electrical-Electronics Engineering in Karabuk University, Türkiye. His research interest include model predictive control, nonlinear control methods, development of control platforms based on FPGA, matrix converters, motor drives, and inverter topologies.



Ugur Ufuk Korpe received his B.Sc. degree in Electrical and Electronics Engineering from Karabuk University, Türkiye, in 2020. He obtained his M.Sc. degree in Electrical and Electronics Engineering from Karabuk University, Türkiye, in 2022. He is currently pursuing his Ph.D. degree in Electrical and Electronics Engineering in Karabuk University, Türkiye. He is currently a Research Assistant in the Department of Electrical and Electronics Engineering at Kirsehir Ahi Evran University. His research interests include model predictive control, control of DC-DC and DC-AC power converters and electric drive applications.